International Journal of Thermal Sciences 215 (2025) 109967

Contents lists available at ScienceDirect

International Journal of Thermal Sciences

journal homepage: www.elsevier.com/locate/ijts

Thermo-hydraulic performance in modified double-layer microchannel heat sinks designs: Optimization of sinusoidal and rectangular fin configurations for enhanced fluid mixing and heat transfer efficiency

Anurag Maheswari [a,*], Yogesh K. Prajapati [b], Arun Uniyal [c], Nitesh Dutt [c], Lalit Ranakoti [d,**], Shubham Sharma [e,f,g,***], A.I. Ismail [h]

[a] Department of Mechanical Engineering, Government Polytechnic Mawana Khurd, Meerut, Uttar Pradesh, 250401, India
[b] Department of Mechanical Engineering, B.I.T. Sindri, Dhanbad, Jharkhand, 828123, India
[c] Department of Mechanical Engineering, COER University, Roorkee, Haridwar, Uttarakhand, 247667, India
[d] Department of Mechanical Engineering, Graphic Era Deemed University, Dehradun, Uttarakhand, 248001, India
[e] Department of Technical Sciences, Western Caspian University, Baku, Azerbaijan
[f] Centre for Research Impact and Outcome, Chitkara University Institute of Engineering and Technology, Chitkara University, Rajpura, 140401, Punjab, India
[g] Jadara University Research Center, Jadara University, Jordan
[h] Mechanical Engineering Department, College of Engineering and Architecture, UMM Alqura University, Saudi Arabia

ARTICLE INFO

Keywords:
Double-layer microchannel heat sink
Intermediate fin
Thermal performance
Pressure drop
Heat transfer
Flow behavior
Optimization

ABSTRACT

A three-dimensional numerical analysis has been performed to investigate the thermo-hydraulic performance of innovative designs of double-layer microchannel heat sinks (DL-MCHS). The conventional DL-MCHS design has been altered by integrating intermediate fins with rectangular and sinusoidal shapes, the latter featuring varying amplitudes (A) and wave numbers (t). These fins are strategically placed along the flow paths within the channel. A comparative evaluation of heat transfer efficiency and pressure drop characteristics between the traditional and modified DL-MCHS designs has been conducted for Reynolds numbers ranging from 100 to 400, and heat flux levels between 500 and 2000 kW/m^2. Single-phase liquid water serves as the cooling medium. The results indicate that the modified designs can enhance heat dissipation by 50–70 % compared to the conventional DL-MCHS. But owing to higher obstructions encountered by coolant in the flow passage, pressure drop penalty also increases in such configurations. Among all the analyzed configurations, the modified DL-MCHS incorporating sinusoidal intermediate fins with an amplitude (A) of 10 μm and a wave number (t) of 5 mm^{-1} demonstrated consistently better thermal performance, achieving approximately 5–10 % higher thermal performance factor compared to the conventional DL-MCHS. Flow visualization of the coolant indicates that the presence of sinusoidal fins promotes improved fluid mixing, which in turn enhances heat transfer. Furthermore, a time-efficient optimization study on DL-MCHS with sinusoidal intermediate fin discloses that heat sink with $A = 10$ μm, and $t = 15.303$ mm^{-1} achieves average Nusselt number ($\overline{Nu}$) ≈ 60–70 % higher than the conventional DL-MCHS.

Nomenclature

A	Wave amplitude [μm]	u_m	Average velocity [m/s]
t	Wave number [mm^{-1}]	W	Channel Width [mm]
A_c	Cross-sectional area [mm^2]		
C_p	Specific heat [J/kg K]		

(*continued on next column*)

(*continued*)

A	Wave amplitude [μm]	u_m	Average velocity [m/s]
D_h	Hydraulic diameter [mm]	*Greek symbols*	
f	Friction factor	ρ	Density [kg/m^3]
$\overline{h}$	Average heat transfer coefficient [W/m^2K]	μ	Viscosity [$Pa.s$]

(*continued on next page*)

* Corresponding author.
** Corresponding author.
*** Corresponding author. Department of Technical Sciences, Western Caspian University, Baku, Azerbaijan.
E-mail addresses: anurag.maheswari@gmail.com (A. Maheswari), lalitranakoti.me@geu.ac.in (L. Ranakoti), shubham543sharma@gmail.com, shubhamsharmacsirclri@gmail.com (S. Sharma).

https://doi.org/10.1016/j.ijthermalsci.2025.109967
Received 24 January 2025; Received in revised form 24 March 2025; Accepted 28 April 2025
Available online 10 May 2025

(*continued*)

A	Wave amplitude [μm]	u_m	Average velocity $[m/s]$
H	Heat sink height $[mm]$		
k	Thermal conductivity $[W/m\,K]$	*Subscript*	
L	Length of channel $[mm]$	b	Bottom
$\overline{Nu}$	Average Nusselt number	c	Channel
p	Perimeter $[mm]$	$conv$	convective
ΔP	Pressure drop $[Pa]$	f	Fin
q	Heat flux $[kW/m^2]$	in	Inlet
Re	Reynolds number	l	Liquid
T	Temperature $[K]$	out	Outlet

1. Introduction

Applications of compact and smaller heat sinks are significantly increasing in the current era of miniaturization of various devices especially electronic components. High performing and efficient systems of the compact size is the need of time. Advancement in technology has made it possible to witness such devices in day to day life. The ongoing trend of miniaturization coupled with high-performance demands has posed a significant challenge in dissipating excess waste heat from compact areas. The heat flux to be removed from electronic components and devices is anticipated to reach up to 10 MW/m^2 in the near future [1–3]. Effective temperature management is critical for ensuring the safe operation of electronic systems, as traditional cooling techniques have proven inadequate. To address this issue [4], introduced microchannel heat sinks (MCHS) as a dependable solution for dissipating high heat flux from limited spaces. Compared to traditional heat sinks, MCHS improve the overall heat transfer rate by significantly increasing the surface area-to-volume ratio. In order to further increase the heat dissipation potential, extensive experimental and numerical works have been reported in the literature pertaining to MCHS. A review of the literature highlights the adoption of various strategies to enhance heat sink performance. These include alterations in channel geometry or shape, innovative heat sink designs, modifications to coolant flow behavior (encompassing single-phase and two-phase flows), selection of coolant types, surface texture and morphology adjustments, improvements in inlet and outlet plenum design, optimization of operating conditions, and active methods such as vibration and electrostatic field application [5–9]. Among these, single-layer microchannel heat sinks (SL-MCHS) have shown considerable potential for managing high heat flux. However, a key drawback of SL-MCHS is the significant temperature gradient along the bottom wall. While higher coolant flow rates could mitigate this issue, they come with the trade-off of increased pumping power, noise, and coolant volume requirements [10,11]. To overcome these issues, researchers have proposed the double or multiple layer heat sinks.

Vafai et al. (1999) introduced the concept of a multilayer microchannel heat sink. Their findings revealed that double-layer microchannel heat sinks exhibit lower thermal resistance and improved heat transfer rates compared to single-layer designs. This enhancement is attributed to the increased coolant flow between the channel walls. Subsequently, several researchers studied and analyzed DL-MCHS to further enhance its overall thermal performance. Influence of increasing the number of layers (more than two layers or multi-layer MCHS) is also investigated [12,13] to recognize their performance pertaining to heat transfer rate [12,13]. [14] numerically investigated MCHS with tapered channels. Results show that the thermal performance enhances with higher convergence angle of the tapered channel. [15] conducted a numerical analysis of double-layer microchannel heat sinks (DL-MCHS) featuring tapered and converging channels. Their study revealed that compared to straight channels, thermal performance was better however, more pumping power was required with the increase in contraction ratio. They observed that Nusselt number increases with the addition of nanoparticles. Patel et al. (2021) have done numerical and experimental investigations of the double-layer mini channel with variable channel width. The findings indicate approximately a twofold improvement in thermal performance compared to the conventional configuration. Zhang et al. [16] conducted a numerical investigation to assess the impact of using thinner and more densely packed fins in the upper channel as opposed to the lower channel. Their findings revealed a 9.42 % decrease in thermal resistance when compared to conventional DL-MCHS designs. Shen et al. (2018) carried out a numerical analysis of wavy and straight staggered DL-MCHS configurations, demonstrating that straight staggered designs provide superior overall thermal performance. Jing et al. (2018) observed that increasing the inlet velocity and the thickness of vertical ribs effectively reduces the thermal resistance in staggered DL-MCHS. Additionally, [17] numerically analyzed the impact of sinusoidal pathways and cavities along the microchannel walls of DL-MCHS, utilizing water nanofluid/GNP–SDBS as the cooling medium. [18] numerically simulated the heat sink configuration with staggered cavities in double-layered. Authors noted enhanced heat transfer with better fluid mixing due to jet and throttling effects. [19] performed the comparative analysis with divergent and convergent channels in double layer microchannel heat sink. It was found that diverging microchannel exhibits higher thermal entropy whereas convergent microchannel has better frictional entropy. [20] numerically analyzed a DL MCHS that possess multi-circuit nested loop (ML). Proposed configuration reduces the peak temperature of the solid substrate by 34 K [21]. experimentally investigated the single layer heat sink and curved double layered heat sink with nanofluids. Authors observed high temperature zones in curved double layered heat sink as compared with conventional DL MCHS. [22] studied the thermohydraulic performance of wavy, tapered DL MCHS with height tapering. Results show that wavy tapered DL MCHS deliberates 13.6 % improved overall performance as compared to the conventional configuration. Goosheneshin et al. [23] conducted an experimental investigation on a cylindrical microchannel heat sink with sinusoidal fins and reported a 6–40 % improvement in Nusselt number compared to straight fins. This improvement was attributed to enhanced convective surface area and improved fluid mixing. While their setup differs from the present DL-MCHS design, the observed performance trends highlight the potential benefits of sinusoidal fins in microchannel heat sink applications.

Above discussion evidently represents that channel geometry is one of the vital features that affects the thermo-hydraulic performance of the DL-MCHS. To maximize the thermal performance of microchannels, many researchers have concentrated on optimizing their geometric design. Commonly employed optimization techniques include the genetic algorithms, simplified conjugate-gradient method, and the inverse problem method [24–27]. Additionally, the response surface methodology (RSM), known for its time efficiency, is frequently utilized to fine-tune critical geometric parameters. Zhou et al. (2016) optimized the wavy MCHS using combination of both RSM and finite volume method (FVM). Results represent 2.8 times more heat transfer in the optimized case. In a study by Zhou et al. (2020), they examined DL-MCHS with adjustable ratios of upper to bottom channel height ($\propto$) and varying channel inclinations (θ). Both parameters were optimized through the use of the RSM. The optimized configuration, with $\propto$ set to 2 and θ to 6°, demonstrated a 34.6 % improvement in thermal resistance compared to single-layer microchannel heat sinks. Additionally using RSM, [28] optimized the micro-mixer; resulting, mass transport was improved besides 33 % reduction in the channel length was reported. Moreover, several researchers also used RSM in combination with numerical and experimental works to optimize the different parameters so that better thermo-hydraulic performance of the heat sinks could be achieved [29–31].

Above discussion reveals that the thermal performance of DL-MCHS is superior as compared to conventional MCHS and it also holds certain additional merits such as better bottom wall's temperature uniformity and lesser thermal resistance. It is to be noted that enormous works have been reported pertaining to conventional MCHS, however, there is scarcity of investigations made over DL-MCHS. Moreover, such

configurations of the heat sinks are less explored as far as design amendment is concerned. Considering these facts, the present numerical work has been executed with an objective to recognize the heat dissipation potential and fluid flow behaviour of the DL-MCHS by incorporating the intermediate fins in the coolant flow passages. Present work also aims to optimize the proposed configuration using appropriate optimization technique. To achieve the objectives, two modified DL-MCHS's configurations with intermediate sinusoidal and rectangular fins are proposed. An inclusive study over thermo-hydraulic performance of the proposed heat sinks is conducted and results are compared with conventional DL-MCHS. Further, to identify the superior configuration among the considered cases, dual response surface-desirability optimization study is also presented.

2. Geometric descriptions of the heat sink

For this simulation, a 3D model of the double-layer microchannel heat sink (DL-MCHS) was developed and analyzed numerically. The "double-layer" configuration involves stacking two distinct layers of channels—upper and lower—over one another, as depicted in Fig. 1. The dimensions of the DL-MCHS used in the analysis are 12 mm in length, 10 mm in width, and 1.4 mm in height ($L \times W \times H = 12 \times 10 \times 1.4$ mm^3). The inlet hydraulic diameter (D_h) of each channel is 0.3 mm.

Both the bottom and upper channels have a height of 0.6 mm, and the thickness of the base and sidewalls is 0.1 mm. This study evaluates five distinct DL-MCHS configurations, which are outlined as follows.

(1) Conventional double-layer microchannel heat sink (CDL-MCHS)
(2) DL-MCHS featuring an intermediate rectangular fin (IRF)
(3) DL-MCHS incorporating an intermediate sinusoidal fin (ISF)

Wave amplitude (A) and wave number (t) of ISF configuration is varied hence, three different cases of this heat sink are simulated which are named as mentioned below.

(3.1) ISF having $A = 10$ μm and $t = 5$ mm^{-1} (ISF-1)
(3.2) ISF having $A = 10$ μm and $t = 35$ mm^{-1} (ISF-2)
(3.3) ISF having $A = 50$ μm and $t = 35$ mm^{-1} (ISF-3)

While developing the sinusoidal fin profiles (ISF-1, ISF-2, and ISF-3), following equation has been employed; $z = A \sin(t.x)$, Where, A is Amplitude of the sinusoidal wave (measured in mm), t is wave number (measured in mm^{-1}), x is x-coordinate along the flow direction, z is z-coordinate representing the fin profile's displacement in the vertical

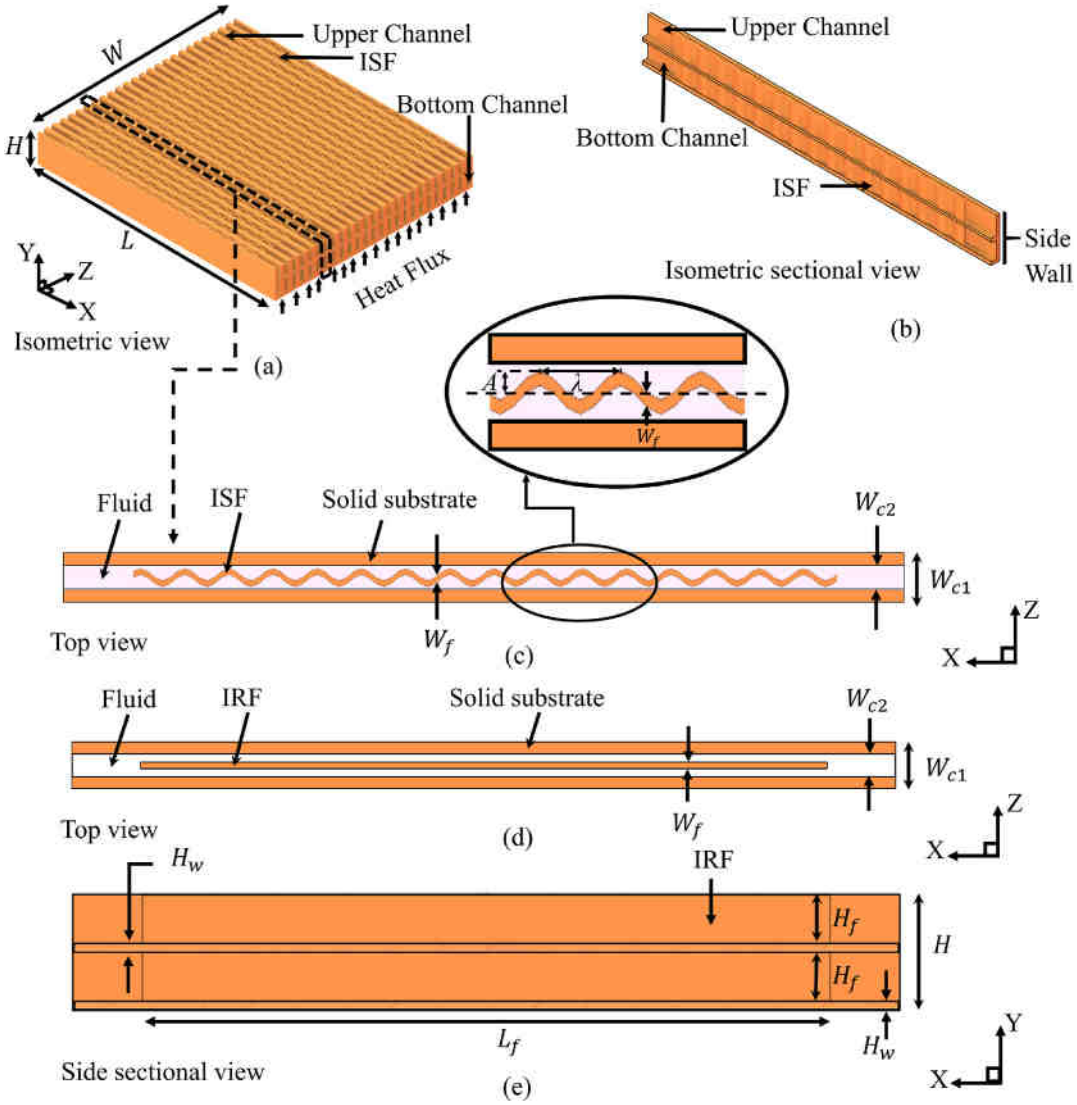

Fig. 1. Schematic of the proposed double-layer microchannel heat sink (a) isometric view (b) sectional isometric view of ISF channel (c) top view of single ISF channel (d) top view of single IRF channel (e) side sectional view of IRF channel.

direction. The corresponding wavelength can be calculated as: $\lambda = 2\pi/t$, i.e $\approx$ 1.257 mm and 0.179 mm for t = 5 mm^{-1} and t = 35 mm^{-1} respectively. It is noteworthy that modified DL-MCHS includes one configuration an intermediate rectangular fin and three distinct profiles of sinusoidal fins (ISF) as mentioned above. These fins are positioned at the center of both the upper and lower channels, as illustrated in Fig. 1 (b) and (c). Due to the fixed channel width constraint, the maximum wave amplitude is set up to 50 μm, whereas minimum wave amplitude is 10 μm. Additionally, the range of wave numbers is chosen to make it easier to generate a smooth ISF profile. When the value of the wave's wave number is high, the processing time necessary to produce a smoother sinusoidal profile increase. The length of the sinusoidal fin (L_f) is 10 mm along the x-axis, and its cross-sectional dimensions are 0.05×0.6 mm^2 in the y-z plane. The fin's span, as shown in Fig. 1(d), extends from 1 mm downstream of the inlet to 1 mm upstream of the outlet, ensuring complete interaction with the coolant. This design keeps the hydraulic diameter at the channel inlet unchanged. Likewise, the modified DL-MCHS with a rectangular fin (IRF) is placed centrally within both the upper and lower channels, as depicted in Fig. 1(d) and (e). In this configuration, coolant flows in parallel within both channels of the heat sink, moving in the same direction.

To optimize computational efficiency and take advantage of the symmetry in the design, only one channel has been selected for the simulation, as shown in Fig. 1(c) and (d). The cross-sectional dimensions of the bottom surface of the chosen channel are 12 mm in length and 0.4 mm in width ($L \times W_{c1} = 12 \times 0.4$ mm^2). Both the sidewalls and base of the channel have a thickness of 0.1 mm. Detailed dimensional information for all microchannel configurations is provided in Table 1. Additionally, it's important to emphasize that the fin height matches the channel height across all heat sink designs considered. Furthermore, achieving such precise fin geometries requires reliable manufacturing techniques that ensure dimensional accuracy and structural stability. Established methods such as Direct Metal Laser Sintering (DMLS), Electroforming, and Chemical Etching have been successfully employed in microfabrication to produce thin structures with high precision [32,33]. These techniques provide viable solutions for fabricating the intricate fin design presented in this study.

3. Numerical approach and governing equations

For this analysis, the commercial software ANSYS Fluent 2020 R1 is employed for numerical simulations. This platform has been frequently used in similar studies due to its proven reliability and precision in predicting outcomes for comparable thermal-fluid problems [34,35,36,37]. The simulations are conducted under steady-state conditions with several key assumptions: (i) the flow is steady and laminar, (ii) the fluid remains incompressible, (iii) viscous dissipation is negligible, (iv) a no-slip boundary condition is assumed at all solid surfaces, (v) solid copper substrate holds constant thermophysical properties ($\rho_s = 8978 \frac{kg}{m^3}$, $c_{p,s} = 381 \frac{j}{kg-K}$ and $k_s = 387.6 \frac{W}{m-K}$) and (vi) the outer walls of the system are thermally insulated. Throughout the simulations, water is used as the single-phase coolant. It is important to highlight that the simulations involve both conduction through the solid material and convection in the liquid, along with heat transfer at the solid-liquid interface. As a result, the conjugate heat transfer method in ANSYS Fluent is employed for all simulations. Additionally, two key properties of liquid water—density (ρ_l) and viscosity (μ_l) are temperature-dependent, and their variations are modelled using the following polynomial equations [37], which are integrated into the simulation process [38].

$$\rho_l = -3.604 \times 10^{-3}\, T^2 + 1.876\, T + 758.1214 \quad (1)$$

$$\mu_l = 1.699 \times 10^{-7}\, T^2 - 1.195 \times 10^{-4}\, T + 0.02143 \quad (2)$$

Where, temperature is expressed in Kelvin (K). With the aforementioned assumptions in place, the following governing equations are solved to evaluate the heat transfer rate and fluid flow characteristics.

$$\text{Continuity equation} : \nabla . \vec{V} = 0 \quad (3)$$

$$\text{Momentum equation} : \rho_l \left(\vec{V} . \nabla \vec{V} \right) = -\nabla P + \nabla . \left(\mu_l \nabla \vec{V} \right) \quad (4)$$

$$\text{Energy equation} : \rho_l c_{p,l} \left(\vec{V} . \nabla T \right) = k_l \nabla^2 T \quad (5)$$

For solid substrate the heat conduction energy equation is expressed as:

$$k_s \nabla^2 T_w = 0 \quad (6)$$

In equations (1)–(6) above, the velocity vector is represented by $\vec{V}$, while pressure, thermal conductivity, temperature, density, and specific heat are denoted by P, k, T, q, and c_p, respectively. The subscripts w, l, and s refer to the wall, liquid, and solid substrate, respectively. As previously mentioned, the hydraulic diameter of the channel is computed at the inlet, and it is given by the following expression:

$$\text{Hydraulic diameter } (D_h) = \frac{4A_c}{p} \quad (7)$$

Here, A_c represents the cross-sectional area, and p denotes the perimeter of the single channel at its inlet. Using this information, the Reynolds number (Re) is determined using the equation provided below.

$$Re = \frac{\rho_l u_{in} D_h}{\mu_l} \quad (8)$$

In this context, ρ_l represents the density of the liquid coolant, u_{in} denotes the average inlet velocity of the coolant, and D_h is the hydraulic diameter of the microchannel. The following equation has been utilized to determine the average heat transfer coefficient:

$$\overline{h} = \frac{q \times A_b}{A_{conv}(\overline{T}_{BW} - \overline{T}_l)} \quad (10)$$

In this analysis, A_b refers to the base area of the microchannel heat sink (MCHS), which is the region subjected to the applied heat flux. Meanwhile, A_{conv} represents the actual surface area participating in convective heat transfer. It is important to note that A_b remains constant across all configurations and is valued at 4.795 mm^2. Conversely, the A_{conv} values vary among the configurations, being 35.98 mm^2 for CDL-MCHS, 58.63 mm^2 for IRF, and 58.635 mm^2, 59.289 mm^2, and 71.10 mm^2 for ISF-1, ISF-2, and ISF-3, respectively. The average coolant temperature ($\overline{T}_l$) is determined by taking the mean of its inlet and outlet values, while the average bottom wall temperature is denoted as $\overline{T}_{BW}$. Using the calculated average heat transfer coefficient ($\overline{h}$), the mean Nusselt number ($\overline{Nu}$) is evaluated using Equation (11).

$$\overline{Nu} = \frac{\overline{h} D_h}{k_l} \quad (11)$$

Table 1
Dimensions of the microchannel heat sink.

Parameter	Value (mm)
Length of heat sink (L)	12
Width of heat sink (W)	10
Height of heat sink ($H = 2H_w + 2H_f$)	1.4
Single-channel width including side walls (W_{c1})	0.4
Channel width (W_{c2})	0.2
Fin Width (W_f)	0.05
Base wall thickness of both layers (H_w)	0.1
Upper & bottom channel height (H_f)	0.6
Fin length (L_f)	10

where k_l is the thermal conductivity of the coolant. Estimation of friction factor (f) for the heat sinks was done from the equation No. 12.

$$f = \frac{2D_h \Delta P}{L \rho_l {u_m}^2} \tag{12}$$

Here, L denotes the length of the channel, ρ_l corresponds to the coolant's density, u_m represents the mean velocity of the fluid, and ΔP signifies the pressure drop measured along the channel length.

3.1. Boundary conditions and solution methodology

Uniform heat flux (q) is imposed on the bottom wall of the heat sink, while all other walls are treated as thermally insulated (adiabatic). The boundary conditions include a velocity inlet and a pressure outlet at the channel's entry and exit, respectively. The coolant is assumed to enter the channel at a uniform temperature of T_{in} =*300 K*. To address the problem, the momentum and energy equations are discretized using a second-order upwind scheme for improved accuracy. The SIMPLEC algorithm is employed to efficiently handle the coupling between pressure and velocity, ensuring faster convergence. The solution process begins with standard initialization from the inlet. The convergence thresholds are established as 10^{-6} for continuity and momentum equations, and 10^{-8} for the energy equation.

Fig. 2 presents the structured Cartesian mesh developed for the computational domain, highlighting the distinction between solid and fluid regions in the ISF heat sink configuration. To validate the mesh suitability, a grid independence analysis was performed by assessing various element sizes. Table 2 summarizes the different grids generated for IRF and ISF heat sinks. Fig. 3(a) illustrates the variation in predicted pressure drop for the IRF profile with decreasing element size at Re = 100 and $q = 1000$ kW/m^2, while Fig. 3(b) shows the variation in average bottom wall temperature for the ISF-1 profile at Re = 300 and $q = 1500$ kW/m^2. Results indicate that when the element size decreases beyond 0.04 mm, variations in both pressure drop and average bottom wall temperature become negligible, with discrepancies limited to approximately 1–1.2 %. This confirms that further grid refinement has minimal impact on the results. Consequently, a grid size of 0.03 mm was selected for all heat sink configurations in the numerical simulations.

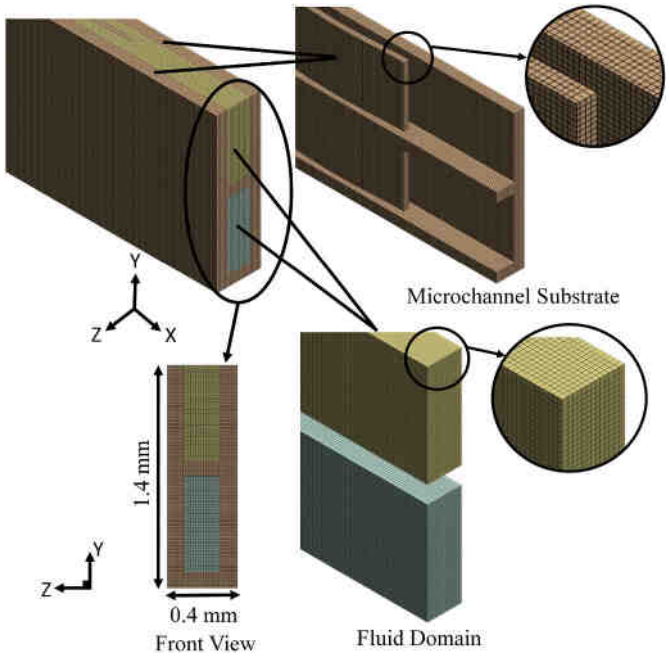

Fig. 2. Meshing of the microchannel heat sink with intermediate sinusoidal fin.

Table 2
Mesh size used in grid independency test of IRF and ISF-1 configuration.

Element size (mm)	0.045	0.040	0.030	0.0275	0.0250	0.0225

3.2. Validation of the numerical model

To validate the current numerical model, the methodology discussed earlier was employed to replicate the experimental and computational studies conducted by Wei et al. (2007). The geometry, operational settings, and boundary conditions of the heat sink were kept identical to those in their work. In this study, only the microchannel section was simulated, excluding the complex manifold structure present in the reference study (Wei et al., 2007). To replicate realistic inlet conditions, a uniform velocity inlet was imposed based on the experimental flow rates in the reference study. A pressure outlet condition was applied at the channel exit to allow natural pressure distribution. The bottom heated surface was subjected to a uniform heat flux, while the remaining walls were treated as adiabatic. Fig. 4 presents a comparison of the axial temperature distribution along the bottom wall for four coolant mass flow rates: 83 ml/min, 116 ml/min, 147 ml/min, and 177 ml/min, under a uniform heat flux of 70 W/cm^2. The plot reveals a near-linear rise in the average bottom wall temperature ($\overline{T}_{BW}$) along the flow direction. Furthermore, an increase in coolant flow rate leads to a noticeable reduction in the average bottom wall temperature ($\overline{T}_{BW}$). Additionally, the reduced slope of the temperature curves signifies a diminished temperature gradient along the flow path. When comparing numerical predictions to experimental data, the model exhibits a slight tendency to overestimate the temperature, particularly at higher flow rates, with a maximum deviation of approximately 1.8 %. Despite this minor discrepancy, the numerical results align closely and consistently with the experimental observations.

To further validate the accuracy of the current model, temperature contour at the axial location of $x = 5$ mm in the y-z plane is plotted for parallel flow rate. The temperature distribution is compared with the contour plot of Wei et al. (2007) at $q = 70$ W/cm^2 and mass flow rate of 3 ml/min as shown in Fig. 5. To assess the accuracy of the present numerical model, temperature deviation was calculated based on the difference in temperature rise relative to the inlet temperature, using the following expression:

$$Deviation\ (\%) = \frac{[(T_s - T_{in}) - (T_r - T_{in})]}{T_r - T_{in}} \times 100$$

Where T_s is the simulated temperature from the present study, T_r is the corresponding temperature from the reference study (Wei et al. (2007)), and T_{in} is the inlet temperature. An evaluation of the contour plots indicates that the temperature distribution in both cases is nearly identical, with a minimal deviation ranging between 0.1 % and 0.27 %. The temperature profiles exhibit a consistent pattern, rising progressively from the central region toward the outer boundaries in the y-z plane. This comparison underscores the reliability of the current numerical model, affirming its capability to deliver accurate predictions within a tolerable margin of error.

4. Result and discussion

The thermo-hydraulic performance of all the proposed DL-MCHS configurations has been evaluated and compared, focusing on key parameters such as the average bottom wall temperature ($\overline{T}_{BW}$), average Nusselt number ($\overline{Nu}$), pressure drop (ΔP), coolant flow dynamics, and overall performance factor (*TPF*). It should be noted that the average heat transfer coefficient ($\overline{h}$), $\overline{Nu}$ and ΔP are calculated by considering the combined thermal-hydraulic behavior of both upper and lower layers. Conversely, the $\overline{T}_{BW}$ is determined exclusively for the bottom layer to better evaluate heat dissipation performance at the critical heat transfer

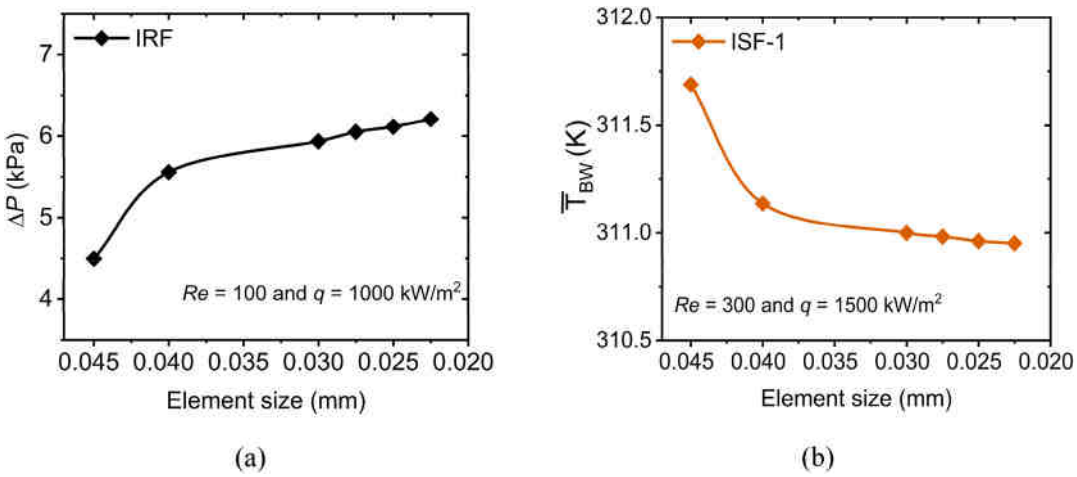

Fig. 3. Variation of (a) ΔP and (b) $\overline{T}_{BW}$ with different grid size.

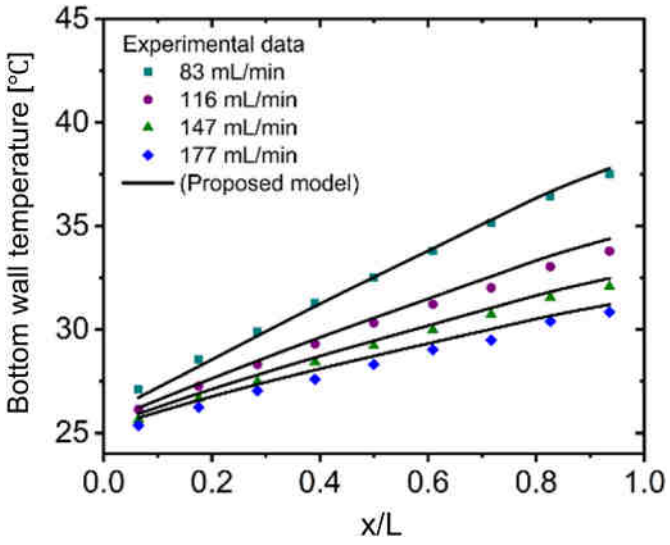

Fig. 4. Comparison of bottom wall temperature distribution with the experimental results of Wei et al. (2007).

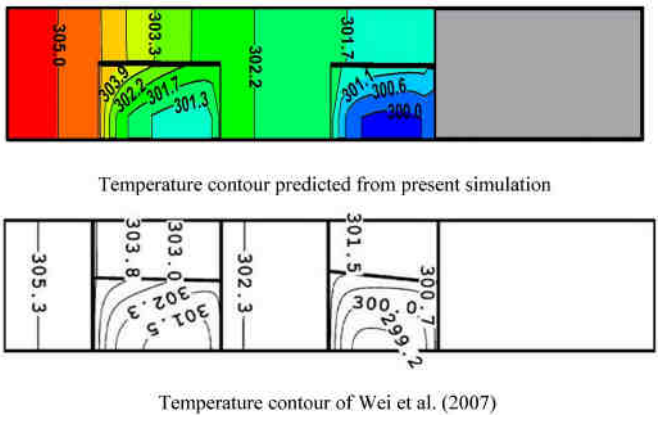

Fig. 5. Comparison of temperature [K] distribution with Wei et al. (2007) in y-z plane at $x = 5$ mm at the flow rate of 83 ml/min.

surface. The analysis considers varying operational conditions, with heat flux ranging from 500 to 2000 kW/m^2 and Reynolds numbers spanning from 100 to 400.

4.1. Heat transfer analysis

Fig. 6(a) illustrates how the area-weighted surface temperature of the bottom wall ($\overline{T}_{BW}$) varies with heat flux (q) across all five configurations of DL-MCHS, evaluated at a Reynolds number of 300. It can be seen that for parallel coolant flow, $\overline{T}_{BW}$ increases linearly with increasing q at a given value of Re besides, it is exceptionally raised for CDL-MCHS configuration. Slope of the curve for this heat sink is steepest as compared to all other cases. Significant rise in bottom wall temperature with q is not desired as it marks the poor heat dissipation from the heat sink. Fig. 6(a) also highlights that modified designs of DL-MCHS with intermediate fin show lesser values of $\overline{T}_{BW}$. Also, compared to CDL-MCHS, rate of increase of $\overline{T}_{BW}$ is moderate with increasing q. This is owing to improved heat transfer because of intermediate fins placed in the heat sink. Availability of the intermediate fins increases the convective heat transfer. Moreover, at lower heat flux, values of $\overline{T}_{BW}$ are almost similar for all the modified configurations; nevertheless at higher heat fluxes, a marginal variation in $\overline{T}_{BW}$ is visible. Among the modified configurations, ISF-3 consistently shows lower $\overline{T}_{BW}$, followed by ISF-2, ISF-1, and IRF. It is to be noted that $\overline{T}_{BW}$ curves for ISF-1 and ISF-2 appear to overlap each other, but closer inspection reveals that ISF-1 has slightly higher values of $\overline{T}_{BW}$. At Re = 300 and $q = 2000$ kW/m^2, highest and lowest values of $\overline{T}_{BW}$ are 328.6 K and 316.5 K respectively in CDL-MCHS and ISF-3 heat sinks. The above comparative analysis indicates that incorporating an intermediate fin enhances heat transfer in comparison with CDL-MCHS. This improvement is primarily due to the expanded convective surface area (≈60–97 %) provided by the modified configurations as compared to CDL-MCHS. Presence of sinusoidal fin in place of rectangular fin slightly favors the better heat transfer due to periodic flow interruption, undulating flow which supports the mixing tendency of the coolant.

Fig. 6(b) illustrate how $\overline{T}_{BW}$ varies with Re at a $q = 1500$ kW/m^2. Plot shows the reduction in values of $\overline{T}_{BW}$ for increasing *Re,* which is obvious because coolant carries out more heat from the solid substrate at higher flow rates. However, all the curves have steeper slopes for lower values of Re which indicates high heat transfer rates—although beyond Re = 200, curves indicate moderated steepness which further reduces. Therefore, from the above illustration, it can be concluded that the heat transfer rate exhibits greater sensitivity and responsiveness at lesser *Re.* Besides, there is a visible difference in the values of $\overline{T}_{BW}$ among the heat sinks for all the values of *Re*. Fig. 6(b) further confirms that the insertion of intermediate fin improves heat transfer rates compared to conventional DL-MCHS. Whereas, performance of all the modified heat sinks is relatively close to each other. It is noteworthy that ISF-3 still has

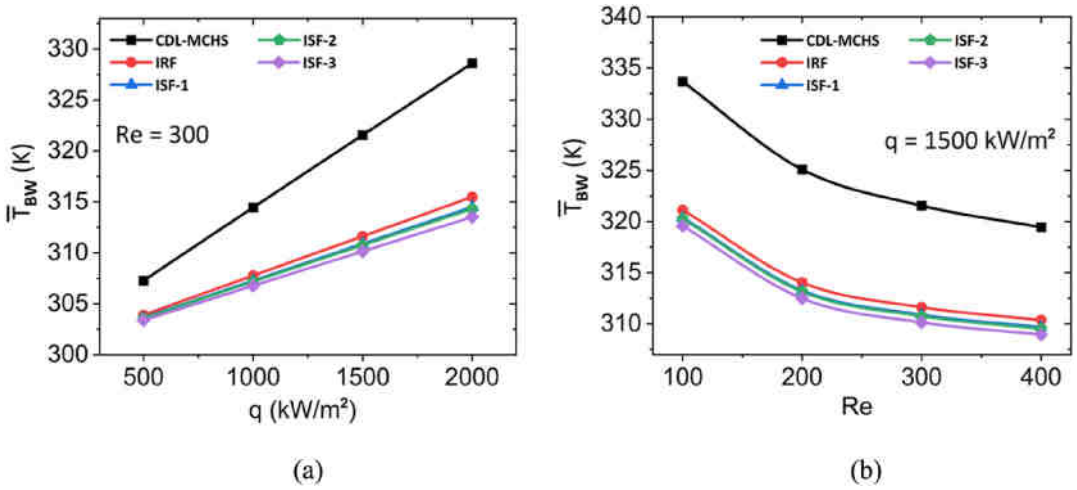

Fig. 6. Variation of $\overline{T}_{BW}$ (a) w.r.t. q at Re= 300, (b) w.r.t. Re at q = 1500 kW/m.^{2}.

minimum values of $\overline{T}_{BW}$ i.e. 319.5 K and 308.9 K Reynolds numbers of 100 and 400, respectively.

Fig. 7(a) depicts the influence of Re on $\overline{Nu}$ for all the considered cases. Regardless of the heat sink design, $\overline{Nu}$ is a strong function of *Re*. Please note that $\overline{Nu}$ has been calculated as per Eqn. no. 11. For a given value of q, $\overline{Nu}$ increases rapidly up to Reynolds number of 200, beyond this range, the rate of increase diminishes, indicating a reduced slope for all the plotted curves. although, $\overline{Nu}$ keeps on increasing moderately with increasing *Re*. It is to be noted that sharp increase in $\overline{Nu}$ up to Re = 200 is consistent with the reduction in $\overline{T}_{BW}$ as discussed in the previous paragraph. Several researchers have recorded similar observations in the study of MCHS [39,37,40]. Moreover, close observation of Fig. 7(a) reveals the following points. Firstly, ISF-1 and ISF-2 demonstrate comparable and superior heat transfer capabilities when measured against the performance of the other heat sink configurations with value of $\overline{Nu}$ lies in the range of ≈16 to 19.4. Additionally, among all the modified configurations, ISF-3 has the maximum convective surface area (71.10 mm^2) still, it deliberates lower $\overline{Nu}$ as compared to its counterparts. Possibly higher wave amplitude (A = 50 μm) of this configuration likely contributed less effectively to enhancing the heat transfer coefficient compared to ISF-1 and ISF-2. This behavior can be better comprehended through the flow visualization analysis presented in the following sections.

Fig. 7(b) represents the effect of heat flux on $\overline{Nu}$ corresponding to fix value of Re = 300 for all five heat sink configurations. It can be noted that irrespective of heat sink, $\overline{Nu}$ remains almost unaffected with increasing values of q. The observed minor variation in $\overline{Nu}$ with increasing heat flux is attributed to the influence of temperature-dependent fluid properties. As heat flux rises, the reduction in viscosity (μ) enhances convective heat transfer, while the reduction in density (ρ) lowers the coolant velocity. These opposing effects partially offset each other, resulting in only slight fluctuations in $\overline{Nu}$. In this plot also, CDL-MCHS consistently shows significantly lower values (≈50–68 % less) of $\overline{Nu}$ compared to remaining cases having intermediate fin. An experimental study conducted by Goosheneshin et al. [23] demonstrated that incorporating sinusoidal fins improves heat transfer performance by a maximum of 40 %, which aligns well with our numerical results showing ≈50–68 % improvement in average Nusselt number when sinusoidal fins are introduced compared to conventional DL-MCHS. Whereas, ISF-1 and ISF-2 show nearly identical and superior heat transfer performance as both the curves overlap for the entire range of heat fluxes. Maximum value of $\overline{Nu}$ in ISF-1 and ISF-2 ranges between 19 and 19.2, which is ≈ 10 % more than ISF-3 and IRF configurations. For the IRF profile, the values of $\overline{Nu}$ remain consistently within the range of 17.2–17.3 across the entire spectrum of heat flux q. The above findings confirm that the introduction of sinusoidal fin with optimal amplitude aids better fluid mixing within the flow passage, resulting in

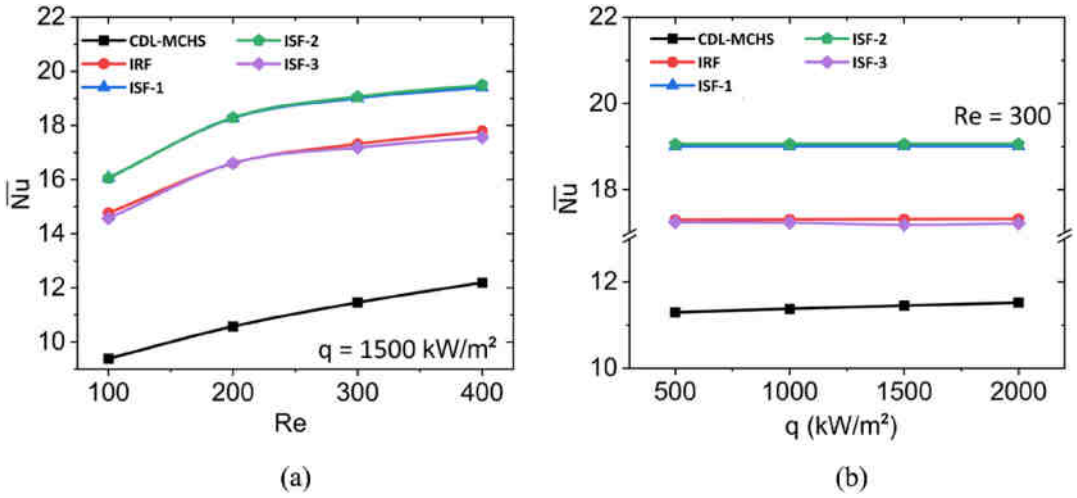

Fig. 7. Variation of $\overline{Nu}$ (a) w.r.t. Re at q = 1500 kW/m^2, (b) w.r.t. q at Re = 300.

improved heat transfer performance. To delve deeper into this phenomenon, a detailed flow visualization of the coolant is presented in the subsequent section.

4.2. Pressure profile

Estimating the pressure drop (ΔP) is crucial for determining the total pumping power needed to sustain coolant flow within the heat sink. This parameter directly influences the operational efficiency and energy consumption of the system. Fig. 8(a) represents the ΔP variation with Re for the fixed value of $q = 1500$ kW/m^2. A common observation is that all the curves (except ISF-3) show the linearly increasing trend of ΔP with increasing value of *Re*. Such type of pressure drop pattern is quite obvious because, increasing Re causes higher mass flow rate and coolant velocity. Least slope of the curve is reported for CDL-MCHS as compared to other modified cases; the order of pressure drop in CDL-MCHS is nearly ≈5 kPa at Re = 400. Modified heat sinks with intermediate fin show higher pressure drop, primarily because of the restrictions offered to the coolant flow in the flow path by the intermediate fin. The pressure drop trends observed in our study are also consistent with the findings of the experimental work by Goosheneshin et al. [23], where the introduction of sinusoidal fins resulted in an increased pressure drop due to enhanced flow resistance.

Among the modified heat sinks, IRF, ISF-1, and ISF-2 have a marginal difference in pressure drop hence; their curves possess almost similar slopes. The pressure drops for IRF, ISF-1, and ISF-2 are ≈25 kPa, 27 kPa, and 31 kPa, respectively, at Re = 400. It is interesting to observe an aberrant variation of ΔP for the ISF-3 heat sink in comparison to remaining heat sinks. ISF-3 configuration has experienced extremely high ΔP ≈300 kPa at Re = 400. It is mainly attributed to higher wave amplitude of the intermediate fin, which resulted in considerably high flow obstruction in the coolant flow path.

Fig. 8(b) illustrates the effect of heat flux on the pressure drop (ΔP) at a Reynolds number of 300. Regardless of the heat sink design, all the curves exhibit minimal variation in pressure drop, which decreases in a linear fashion as the heat flux (q) increases. It is important to note that at higher heat fluxes, coolant temperature is comparatively high which leads to reduction in its density. Since pressure drop is directly proportional to the density (as per Darcy–Weisbach equation) hence, it exhibits decreasing trend with the heat flux. Moreover, for a specific value of *Re*, the pressure drop (ΔP) varies notably across different heat sink configurations. It is absolutely clear from the plot that IRF offers the lowest ΔP among the modified heat sinks, which ranges between 19.4 and 17.5 kPa, followed by ISF-1 (20.8–19.1 kPa) and ISF-2 (23.6–21.9 kPa). As mentioned earlier, maximum pressure drops encounters in ISF-3 which falls in between 205 and 198.2 kPa.

4.3. Thermal performance factor

Evaluating the overall thermal efficiency of the modified DL-MCHS in comparison to the CDL-MCHS is crucial for understanding its heat transfer benefits relative to the additional pressure drop. This comparison is facilitated by the thermal performance factor (*TPF*), which quantifies the heat transfer improvement relative to the increased friction factor in the modified configurations compared to the conventional CDL-MCHS. The *TPF* is expressed as follows:

$$TPF = \frac{\left(\frac{\overline{Nu}}{\overline{Nu}_o}\right)}{\left(\frac{f}{f_o}\right)^{\frac{1}{3}}} \tag{13}$$

In the above equation, values of $\overline{Nu}_o$ and f_o belong to the CDL-MCHS (reference configuration). It is acknowledged that compared to reference heat sink i.e., CDL-MCHS, if the modified configurations deliberate $TPF > 1$, it indicates that overall thermal performance was improved [41]. Thereby, modifications made in the heat sink could be justified. Fig. 9(a) illustrates how the *TPF* varies with Re at a heat flux of 1500 kW/m^2. The results show that the modified heat sink configurations: ISF-1, ISF-2, and IRF have shown increasing values of *TPF* up to Re = 200. Beyond that, because of the high-pressure penalty, *TPF* decreases as the curves show negative slopes of *TPF* with increasing *Re.* ISF-1 holds $TPF > 1$ for the entire range of *Re,* the maximum value of *TPF* for ISF-1 has been recorded ≈1.08 at Re = 200, followed by ISF-2 and IRF. Fig. 9 (a) further indicates that for ISF-2 and IRF configurations, the thermal performance factor (*TPF*) falls below unity once the Reynolds number exceeds 350 and 300, respectively. This signifies a decline in the thermal performance of these heat sinks as the Reynolds number increases. It is worth mentioning that ISF-3 shows *TPF* substantially smaller than unity which further decreases with increasing *Re*. *TPF* values for ISF-3 is ranging from 0.57 to 0.47.

Fig. 9(b) illustrates the relationship between the thermal performance factor (*TPF*) and heat flux (q) at a Reynolds number of 300. It is evident that, regardless of the heat sink configuration, all the curves exhibit a slight decreasing trend as the heat flux increases. As noted above, among all the heat sink configurations, ISF-3 exhibits the lowest thermal performance due to the high-pressure drop penalty. Nevertheless, ISF-1 and ISF-2 have $TPF > 1$ for the considered ranges of q. Additionally, *TPF* of ISF-2 approaches to unity beyond the heat flux q = 1500 kW/m^2. Besides, Fig. 9(b) illustrates that IRF configuration

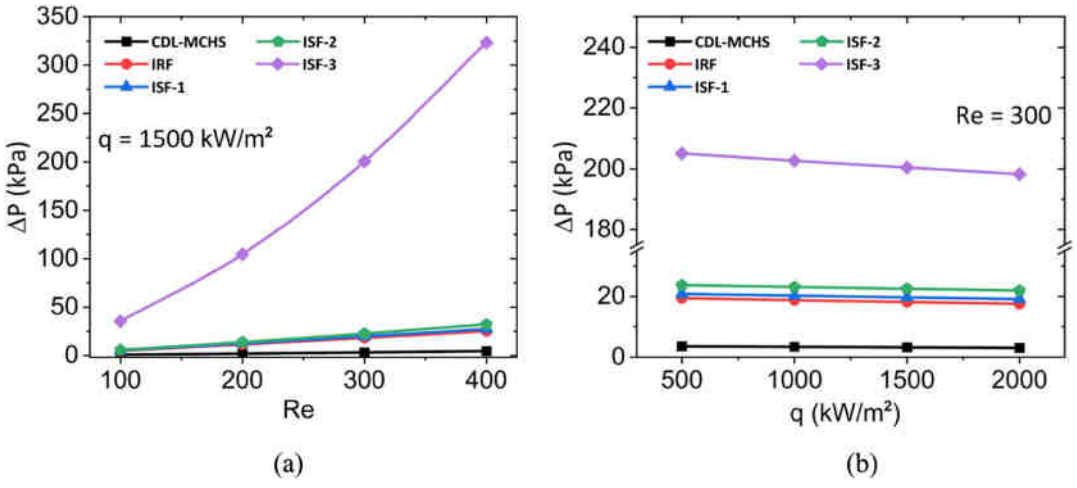

Fig. 8. Variation of pressure drop (a) w.r.t. Re at q = 1500 kW/m^2 (b) w.r.t. q at Re = 300.

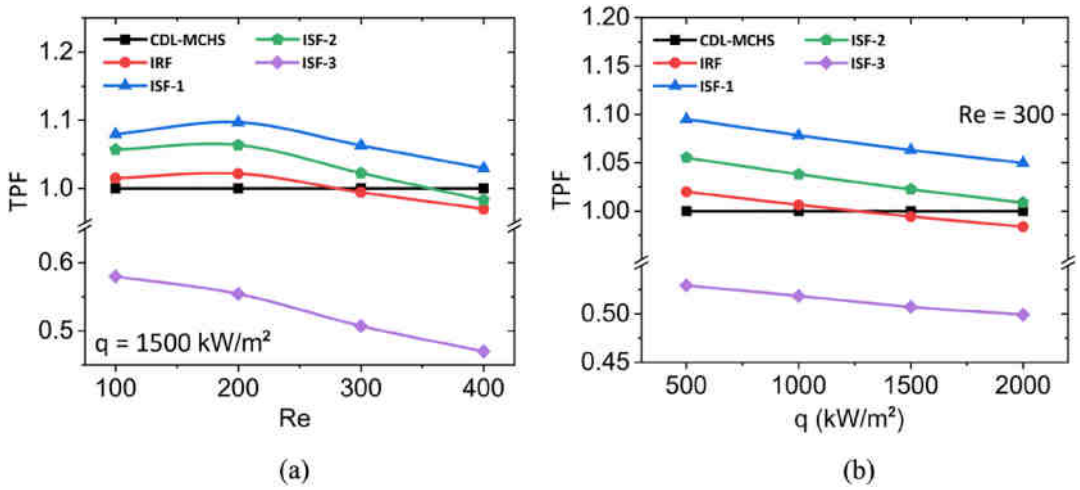

Fig. 9. Variation of *TPF* (a) w.r.t. Re at $q = 1500$ kW/m^2, (b) w.r.t. q at Re = 300.

performs better for lower values of q; however, beyond $q = 1000$ kW/m^2, thermal performance of IRF heat sink degraded as *TPF* approaches lesser than one. Based on the observations, it may be concluded that by keeping the constant wave amplitude (A= 10 μm), heat sink with the lower wave number (t) i.e., ISF-1 with $t = 5$ mm^{-1} performs better as compared to higher t as evident for ISF-2 with $t = 35$ mm^{-1}. Furthermore, please note that variation in A keeping t constant may also influence heat sinks's total thermal performance. Say, for $t = 35$ mm^{-1}, ISF-2 with lower wave amplitude ($A = 10$ μm) has superior performance than ISF-3 having higher wave amplitude value, i.e. $A = 50$ μm. Owing to high wave amplitude, higher flow obstructions are offered and flow passage are more confined with considerable undulation in the flow path. Hence, conclusion may be drawn that wave parameters including, (i) wave amplitude and (ii) wave number, are affecting the overall thermal performance of the intermediate sinusoidal heat sinks. Therefore, both the parameters (A and t) may be optimized to identify the superior heat sink design.

5. Optimization of the ISF heat sink

So far, it is found that ISF-1 and ISF-2 configurations consistently deliberated better thermal performance compared to their counterparts. Therefore, it was decided to optimize the ISF configuration using a time-efficient response surface methodology (RSM). RSM has been widely employed to optimize experimental responses. Further, it has been expanded to cover numerical results, helping to minimize computational costs and time [42,43]. Relationship between desired responses and input parameters is expressed as:

$$\eta = \beta_0 + \sum_{i=1}^{k} \beta_i x_i + \sum_{i=1}^{k} \beta_{ii} x_i^2 + \sum_{i=1}^{k} \sum_{j=1}^{k} \beta_{ij} x_i x_j|_{i<j} \quad (14)$$

In this context, x_i and x_j signify the independent design parameters, while β_0 denotes the predicted response at the midpoint of the simulation setup. The coefficients β_i, β_{ii} and β_{ij} correspond to the linear, quadratic, and interaction effects between the variables, respectively. Additionally, k indicates the total count of independent design parameters under consideration.

To strategize the numerical simulation, central composite design (CCD) is opted. Total proposed CCD cases can be calculated using the formula:

$$N_D = n_f + n_a + n_c \quad (15)$$

Where, $n_f = 2^k$ corner or factorial points, $n_a = 2k$ star or axial points, and n_c = centre points [31].

Based on the above comprehensive discussion, heat sink configurations with sinusoidal fin have been selected for optimization using the desirability approach. The response functions selected for optimization are *TPF* and $\overline{Nu}$, both of which are directly influenced by the convective surface area (A_{conv}), The value of (A_{conv}), in turn, is governed by the following factors:

i. Wave amplitude (A) of sinusoidal fin
ii. Wave number (t) of sinusoidal fin

To optimize the ISF configuration, the parameters A and t are chosen as the independent input variables. Table 3 outlines the range of these variables and the boundary conditions used in the numerical simulations. As highlighted earlier, identifying the best combination of A and t is crucial for designing a high-performance heat sink, as both significantly influence its overall thermal behavior. The results of *TPF* and $\overline{Nu}$ for all nine scenarios suggested by the CCD approach, featuring various values of A and t, are detailed in Table 4.

Fig. 10 depicts the streamline plots for all nine proposed cases at Re = 200 and $q = 1000$ kW/m^2. It is evident that at moderate values of A and t, coolant flow is smooth wherein fluid traces the waviness of the fins. Undulation of the fin is propagated in the bulk fluid motion causing zig-zag motion and improved mixing. However, for higher values of $A \geq 30$ and $t \geq 20$, as shown in the cases 6, 8 &9 wave peak is more pertinent, causing severe flow disturbance and formation of eddies. It also illustrates that vortices are more likely to appear under larger A and higher t. Nevertheless, such profiles offer significantly higher pressure drop causing degradation in overall thermal efficiency of the heat sink. Due to the geometric limitation imposed by the fixed channel width (0.2 mm in present study) at higher amplitudes and wave numbers, coolant gets trapped inside the intermediate fin profile and smooth flow is hindered which resulted in lower heat transfer rate. Table 4 lists the *TPF* and $\overline{Nu}$ for all the considered cases. Heat sinks with the least wave amplitude A = 10 μm shows increasing *TPF* with decreasing wave number. Case 1 (ISF-1, $A = 10$ μm, $t = 5$ mm^{-1}) has a maximum value of *TPF* ≈1.113 followed by case 4 and case 6. Besides, case 2 shows the maximum value

Table 3
Numerical simulation range of ISF.

Working condition	Description
A	10–50 μm
t	5–35 mm^{-1}
q	1000 kW/m^2
Re	200

Table 4
Variation of *TPF* and $\overline{Nu}$ across various CCD configurations under operating conditions of $q = 1000$ kW/m^2 and Re = 200.

Design Case No.	A [μm]	t [mm^{-1}]	*TPF*	$\overline{Nu}$
1 (ISF-1)	10	5	1.11385	18.2730
2	30	5	0.99970	18.5925
3	50	5	0.77874	17.9961
4	10	20	1.10204	18.3837
5	30	20	0.91328	18.1912
6	50	20	0.67341	17.7131
7 (ISF-2)	10	35	1.08126	18.2884
8	30	35	0.80631	17.6676
9 (ISF-3)	50	35	0.56660	16.6160

of $\overline{Nu} \approx 18.59$.

Fig. 11 illustrates the bottom wall temperature contours for various heat sink configurations, including CDL-MCHS, under conditions of Re = 200 and $q = 1000$ kW/m^2. The coolant flows from left to right, as indicated by the directional arrow. Despite differences in heat sink designs, all cases exhibit a comparable temperature distribution trend, characterized by a progressive rise in temperature along the flow path. Results show that CDL-MCHS has maximum bottom wall temperature ranges from 310.4 to 321.4 K with the highest temperature gradient.

However, for all the ISF cases, temperature values lie in the range of 305–314 K. Therefore, it can be concluded that ISF heat sinks exhibit a lower temperature gradient across their bottom wall, facilitating more efficient heat dissipation than the CDL-MCHS configuration. Furthermore, it is evident from Fig. 11 that different combinations of A and t, are not much affecting the temperature distribution pattern and its values. Fig. 12 presents the values of the average Nusselt number and pressure drop for each of the cases under consideration. It is interesting to note that compared to wave number, pressure drop in more sensitive to wave amplitude. Increasing value of A is more responsible for the higher pressure drop than t.

From the findings derived from the RSM analysis in Table 4 and Fig. 12, following second-order polynomial regression equations for *TPF* and $\overline{Nu}$ are obtained:

$$TPF = 1.1819 - 4.59\,A + 0.00054\,t - 51.1\,A^2 - 0.000023\,t^2 - 0.1496\,A \times t \quad (16)$$

$$\overline{Nu} = 17.793 + 42.2\,A + 0.0433\,t - 680\,A^2 - 0.000846\,t^2 - 1.163\,A \times t \quad (17)$$

Fig. 13 illustrates how the *TPF* response varies with the wave parameters A and t, while maintaining constant values of $q = 1000$ kW/m^2 and Re = 200. The data reveals that as A and t decrease, the *TPF* value increases. This can be explained by the fact that at lower values of A and t, lesser pressure drop occurs in the channel. Moreover, Fig. 14 shows, variation of $\overline{Nu}$ with A and t. Value of $\overline{Nu}$ also increases with decreasing

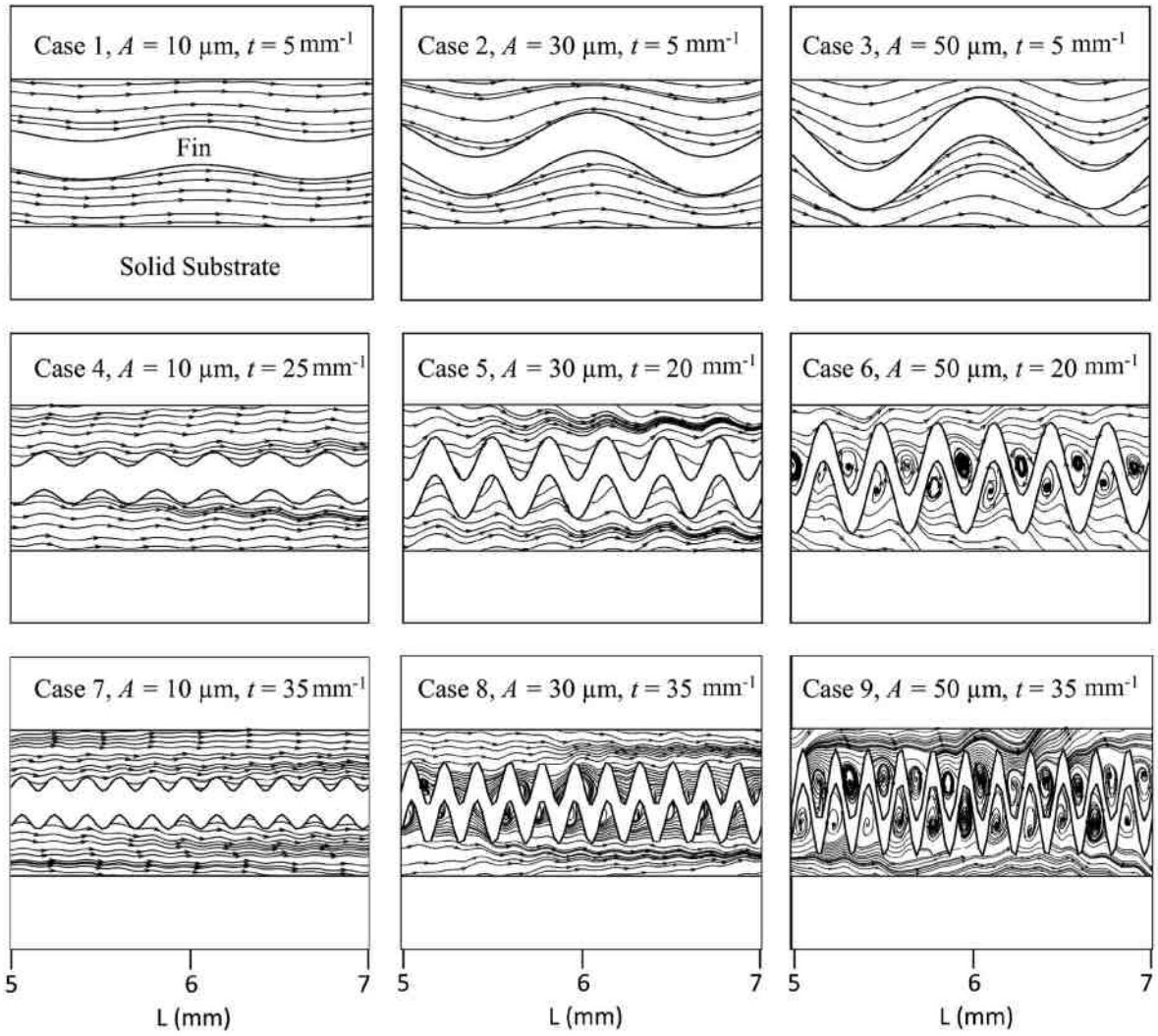

Fig. 10. Streamline plot for a section in z-x plane at y = 0.4 mm from the bottom at Re = 200, $q = 1000$ kW/m^2 for all cases proposed by RSM.

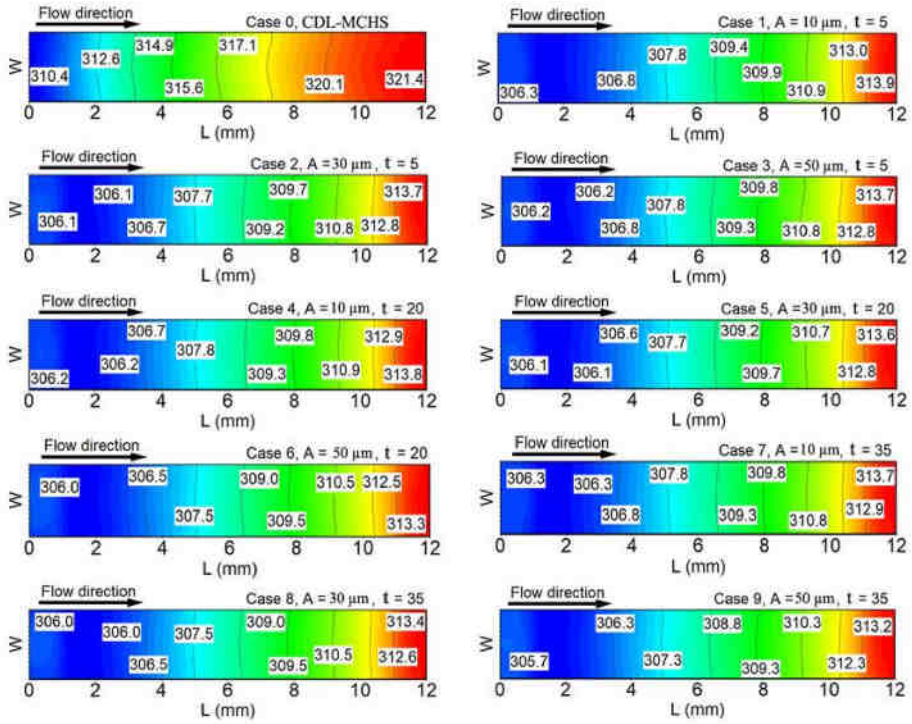

Fig. 11. Temperature contour of bottom wall at Re = 200, q = 1000 kW/m^2 for all the cases proposed by RSM.

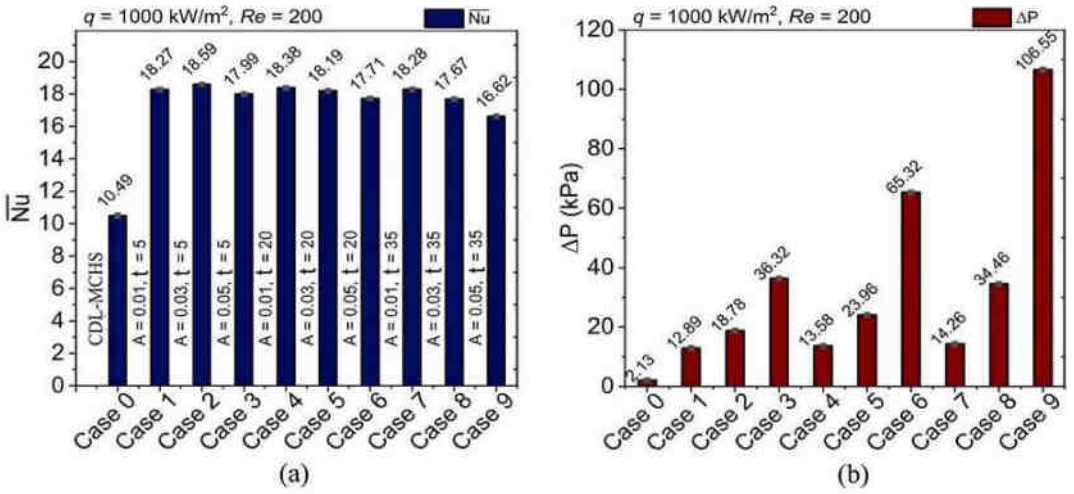

Fig. 12. Effect of wave amplitude (A) and wave number (t) for different DL-MCHS with intermediate sinusoidal fin.

A and t due to favourable fluid flow behaviour.

5.1. Optimization of ISF configuration using desirability approach

In the present optimization study TPF and $\overline{Nu}$ are selected as the response functions. Optimal input variables are assumed to satisfy the optimization conditions which are mathematically expressed as follows:

$$\text{Max} : E(x) = TPF$$

$$\text{Max} : F(x) = \overline{Nu}$$

$$\text{Side constraints} : 10 \le x_1 \le 50$$

$$5 \le x_2 \le 35 \tag{18}$$

Where, x_1 and x_2 represent independent input variables A and t respectively [31].

Application of desirability function to determine the optimal input variable relies on transforming the response y_i into a unique desirability function d_i which is constrained within the:

$$0 \le d_i \le 1 \tag{19}$$

Where, d_i approaches to unity, means the targeted goal is achieved, whereas $d_i = 0$ represents response lies outside the acceptable area [31, 44]. For response y_i where the goal is to maximize T_i, the desirability function is expressed as:

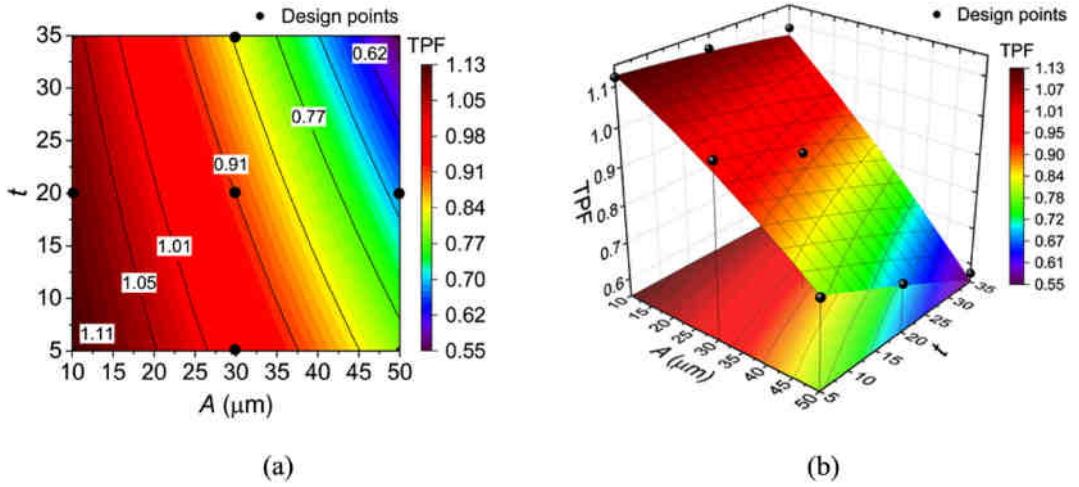

Fig. 13. Variation of *TPF* with *A* and *t* (a) contour plot [2D] (b) surface plot [3D].

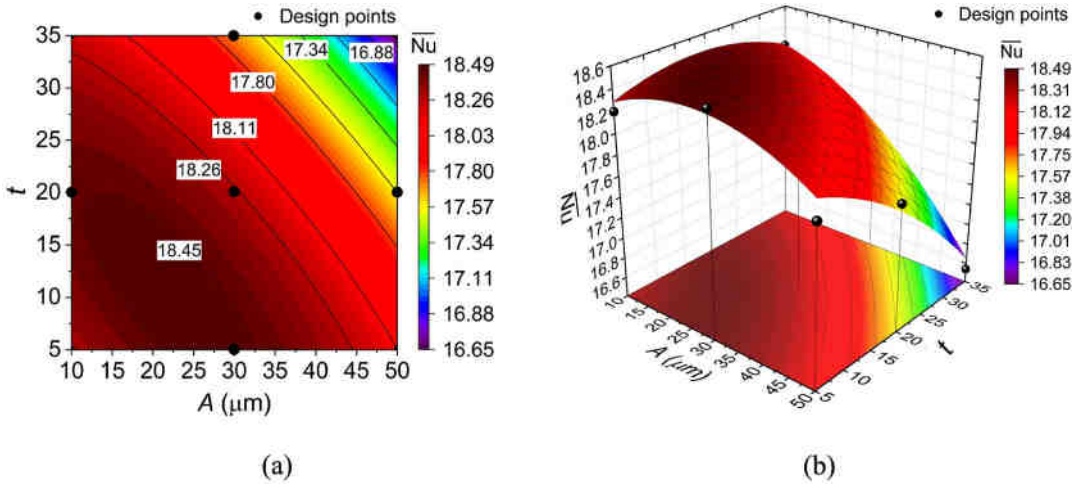

Fig. 14. Variation of $\overline{Nu}$ with *A* and *t* (a) contour plot [2D] (b) surface plot [3D].

$$d_i = \begin{cases} 0 & y_i < L_i \\ \left(\dfrac{y_i - L_i}{T_i - L_i}\right)^r & L_i \le y_i \le T_i \\ 1 & y_i > T_i \end{cases} \tag{20}$$

In this context, L_i denotes the minimum allowable value for the response, while r represents the weighting factor. A value of $r < 1$ indicates reduced sensitivity in the desirability function, $r > 1$ suggests increased sensitivity, and $r = 1$ reflects a balanced sensitivity level [45]. The overall desirability index (D), which combines all individual desirability functions, is calculated as their mean:

$$D = (d_1 d_2 d_3 \ldots d_m)^{\frac{1}{m}} = \left[\prod_{i=1}^{m} (d_i)\right]^{\frac{1}{m}} \tag{21}$$

In this formulation, m represents the total number of response variables, which, for the purposes of this study, is set to $m = 2$. The design variables are strategically selected to optimize the overall desirability index (D), aiming to achieve the most favourable balance across the targeted outcomes [45]

Based on the proposed second-order polynomial regression equations (Eqn. no. 16&17), the desirability functions d_1 and d_2 were chosen to represent the responses for $\overline{Nu}$ and *TPF*, respectively, with both responses set as targets for maximization. A weight factor of $r = 1$ was assigned, ensuring equal significance was given to both responses during the optimization process. The optimization results for the ISF heat sink are illustrated in Fig. 15. In this figure, rows correspond to the response functions being optimized, columns denote the independent design parameters, and the values within each cell reflect the response variation concerning an individual parameter, assuming all other variables remain constant. The vertical solid red colour line shows the value of the current optimal input variable and the horizontal dotted line represents the value of the response function with respect to optimal input variables. Fig. 15 also reveals the values of the composite desirability D along with the individual desirability d_1 and d_2 i.e. 0.9563, 0.91959, and 0.99441, respectively. The obtained desirability values indicate a successful optimization process. Moreover, the plot demonstrates that the optimal response values, achieving maximum desirability, are associated with $A = 10$ μm and $t = 15.303$ mm^{-1}. Predicted outcomes for the responses are also displayed in Fig. 15. Additionally, Table 5 provides a comparison of predicted results, numerically simulated values, and the corresponding relative errors. It is important to highlight that the relative errors remain within an acceptable range, validating the reliability and effectiveness of the employed methodology.

To further elaborate upon the coolant flow characteristics and to better understand the flow physics inside the channel, velocity vectors are analyzed. Fig. 16 provides a comparative analysis of velocity

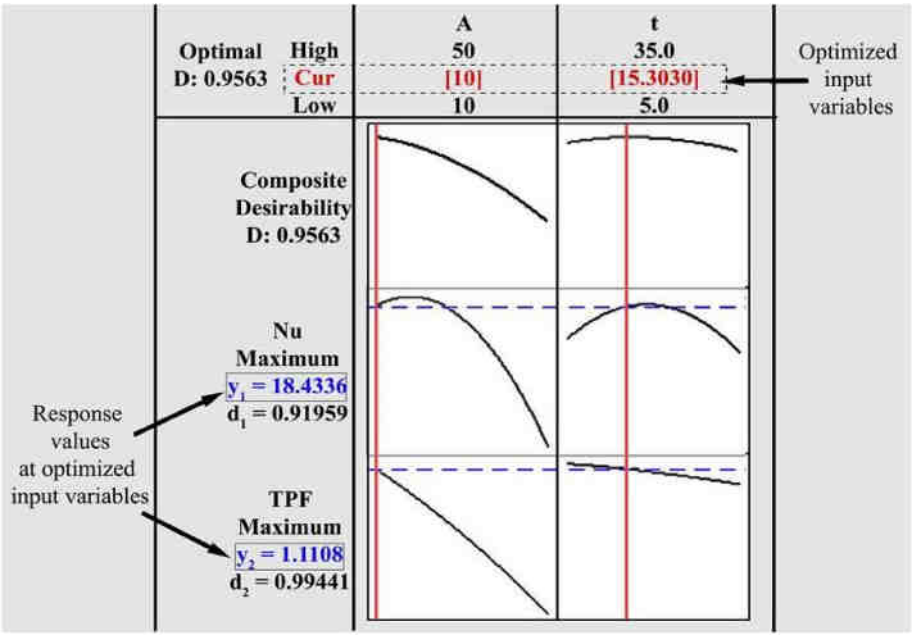

Fig. 15. Optimization results for ISF.

Table 5
Optimization result and comparison of predicted and numerically simulated values.

Optimum inputs		$\overline{Nu}$		*TPF*		Relative errors (%)	
A [μm]	t [mm^{-1}]	Predicted	Numerical	Predicted	Numerical	$\overline{Nu}$	*TPF*
10	15.303	18.4336	18.3227	1.1108	1.1068	0.60	0.36

contours in the *z*-*x* plane for three heat sink configurations: CDL-MCHS, IRF, and the RSM-optimized ISF. These contours, plotted for Re = 400 and $q = 1500$ kW/m^2, illustrate distinct flow characteristics. In the CDL-MCHS configuration (first plot), the coolant exhibits a highly structured flow pattern. Boundary layers form along the sidewalls of the channel and progressively thicken as the flow advances, while the maximum velocity is concentrated at the channel's core. In the second plot, due to the presence of an intermediate rectangular fin, flow bifurcates in two similar flow passages, which leads to the development of thinner boundary layers moreover; coolant was exposed to more heated surface area as compared to previous case. Therefore, it enhances the possibility of better heat transfer rate. Compared to the above-discussed configurations, pattern of velocity distribution is significantly different in the 3rd case having sinusoidal fin. It can be clearly observed from the plot that coolant flow is not ordered due to the waviness of the sinusoidal fin hence, fluid mixing is comparatively better. It also increases the possibility of thinner and intermittent thermal boundary layer. Additionally, alternating regions of elevated and reduced velocity are observed throughout the flow path, with the peak velocity reaching 2.11 m/s. Evolution of such flow behaviour with better coolant mixing and other favourable circumstances support improved thermal performance.

The enhanced performance of the ISF-optimized configuration (A = 10 μm and t = 15.303 mm^{-1}) has been evaluated by comparing its effectiveness in terms of $\overline{Nu}$ and *TPF* against ISF-1, ISF-2 and ISF-3 heat sink designs. Fig. 17 depicts the variation in the $\overline{Nu}$ with Re at a constant heat flux of 1500 W/m^2. The optimized geometry shows a marginal improvement in heat transfer performance compared to ISF-1 and ISF-2 across the examined Re range. ISF-3, on the other hand, exhibits consistently lower $\overline{Nu}$ values, indicating reduced thermal performance. The improved performance of the optimized geometry is attributed to its enhanced flow distribution and heat transfer characteristics. Fig. 18 illustrates the *TPF* variation with Re under identical heat flux conditions. The optimized design achieves *TPF* values comparable to ISF-1, confirming its effective balance between heat transfer enhancement and pressure drop. ISF-3 demonstrates significantly lower *TPF* values, further highlighting its reduced thermal-hydraulic performance. These observations underscore the improved heat transfer and hydraulic performance achieved by the optimized design, aligning with the intended objective of enhancing system efficiency.

6. Conclusions

This study undertakes a detailed numerical comparison of five distinct DL-MCHS configurations, examining heat flux values ranging from 500 to 2000 kW/m^2 and Reynolds numbers spanning 100 to 400. The investigation extensively evaluates overall thermal performance and fluid flow characteristics, utilizing water as the single-phase coolant. The analysis explores the impact of incorporating intermediate fins, both rectangular and sinusoidal, with varying wave amplitudes and wave numbers. The numerical results lead to the following key conclusions.

i. The integration of intermediate fins within the flow passage of modified DL-MCHS results in enhanced heat transfer performance when compared to the CDL-MCHS. Specifically, the IRF configuration demonstrates a reduction of approximately 5 % in the average bottom wall temperature and a significant increase of nearly 50 % in the heat transfer coefficient relative to CDL-MCHS.
ii. Compared to IRF, wavy intermediate fin further enhances the heat dissipate rate. ISF-1 and ISF-2 configurations have shown 9–10 % higher $\overline{Nu}$. This improvement is primarily due to the increased convective surface area, undulating flow behaviour causing better fluid mixing.

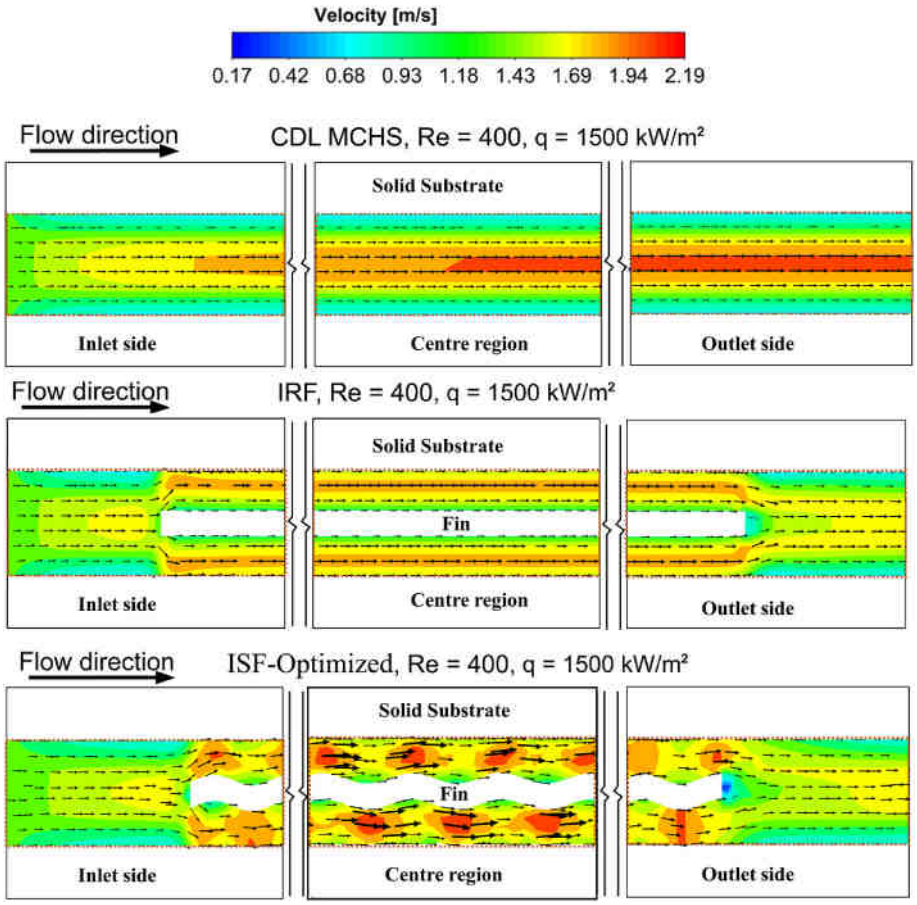

Fig. 16. Velocity vector in z-x plane (y = 0.4 mm from the bottom) at Re = 400 and q = 1500 kW/m.^{2}.

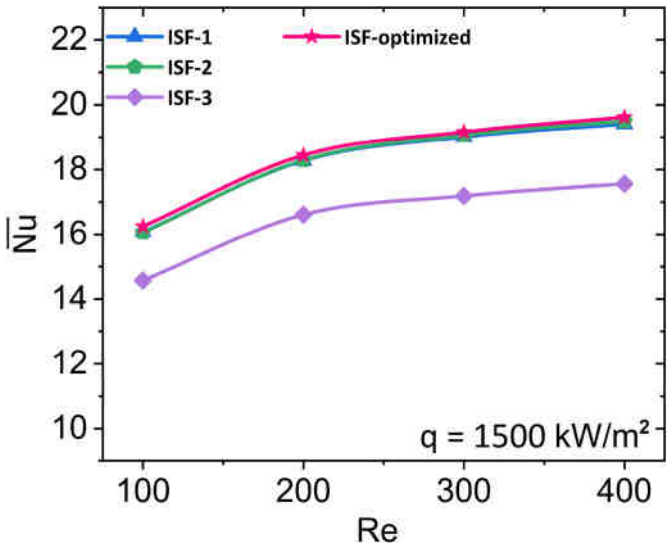

Fig. 17. Comparison of $\overline{Nu}$ of ISF-optimized with other configurations with Re at q = 1500 kW/m.^{2}.

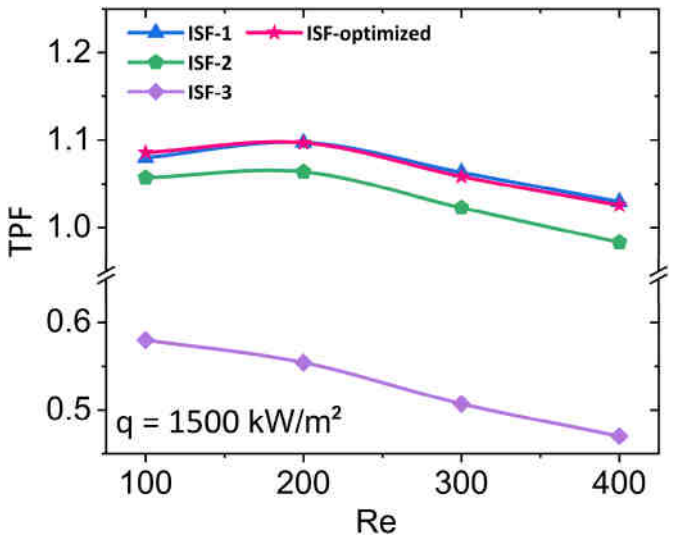

Fig. 18. Comparison of *TPF* of ISF-optimized with other configurations with Re at q = 1500 kW/m.^{2}.

iii. ISF heat sinks offer more restriction to the coolant flow in the flow passage, leading to increased pressure penalty. As the wave amplitude increases, the pressure drop also rises accordingly. Nevertheless, higher pressure drop is compensated by improved heat transfer therefore; thermal performance factor of ISF is more than remaining heat sinks.

iv. As amplitude varies from 10 to 30 μm at t = 20 mm^{-1}, *TPF* decreases by ≈ 21 %. Moreover, an increase in wave number also affects the heat sink's thermal performance, as t varies from 5 to 35 mm^{-1} at A = 10 μm, *TPF* decreases by ≈ 3 %.

v. RSM method is used to optimize the ISF heat sink to obtain maximum heat transfer rate and overall thermal performance. Accordingly, values of optimized wave amplitude and wave

number (t) are 10 μm and 15.303 mm^{-1}, respectively. The optimized ISF achieves the maximum value of $\overline{Nu}$ ≈60–70 % higher than CDL-MCHS. Additionally, its thermal performance is consistently higher than remaining configurations.

CRediT authorship contribution statement

Anurag Maheswari: Conceptualization, Writing – original draft, Supervision, Project administration, Methodology, Investigation, Funding acquisition, Formal analysis. **Yogesh K. Prajapati:** Conceptualization, Writing – original draft, Supervision, Project administration, Methodology, Investigation, Funding acquisition, Formal analysis. **Arun Uniyal:** Conceptualization, Writing – original draft, Supervision, Project administration, Methodology, Investigation, Funding acquisition, Formal analysis. **Nitesh Dutt:** Conceptualization, Writing – original draft, Supervision, Project administration, Methodology, Investigation, Funding acquisition, Formal analysis. **Lalit Ranakoti:** Conceptualization, Writing – original draft, Supervision, Project administration, Methodology, Investigation, Funding acquisition, Formal analysis. **Shubham Sharma:** Writing – review & editing, Formal analysis. **A.I. Ismail:** Writing – review & editing, Formal analysis.

Ethical approval

Not applicable.

Consent to participate

Not applicable.

Consent to publish

All authors have read and approved this manuscript.

Funding

The author extend their appreciation to Umm-Alqura University, Saudi Arabia for funding this research work through grant number: 25UQU4240002GSSR03.

Declaration of competing interest

The authors declare that they have no known competing financial interests or personal relationships that could have appeared to influence the work reported in this paper.

Acknowledgments

The author extend their appreciation to Umm-Alqura University, Saudi Arabia for funding this research work through grant number: 25UQU4240002GSSR03.

Data availability statement

All the characterizations, analysis, testing's related work and testing's has solely been responsible by Anurag Maheswari. Additionally, the raw data can be obtained on request from the corresponding author, Anurag Maheswari.

References

[1] R.R. Schmidt, B.D. Notohardjono, High-end server low-temperature cooling, IBM J. Res. Dev. 46 (2002) 739–751.
[2] R.L. Webb, Next generation devices for electronic cooling with heat rejection to air, J. Heat Tran. 127 (2005) 2–10.
[3] N.H. Naqiuddin, L.H. Saw, M.C. Yew, et al., Overview of micro-channel design for high heat flux application, Renew. Sustain. Energy Rev. 82 (2018) 901–914.
[4] D.B. Tuckerman, R.F.W. Pease, High-performance heat sinking for VLSI, IEEE Electron Device Lett. 2 (1981) 126–129.
[5] Li D, Timchenko V, Reizes JA, et al. Effect of operating frequency on heat transfer in a microchannel with synthetic jet. Comput. Therm. Sci.: Int. J.;1..
[6] Dewangan SK, Sinha SL, Gupta PK. Comparative study of fluid flow and heat transfer in rectangular and wavy microchannel. Comput. Therm. Sci.: Int. J.;9..
[7] A.J. Chamkha, M. Molana, A. Rahnama, et al., On the nanofluids applications in microchannels: a comprehensive review, Powder Technol. 332 (2018) 287–322.
[8] Y.K. Prajapati, P. Bhandari, Flow boiling instabilities in microchannels and their promising solutions–A review, Exp. Therm. Fluid Sci. 88 (2017) 576–593.
[9] T.G. Karayiannis, M.M. Mahmoud, Flow boiling in microchannels: fundamentals and applications, Appl. Therm. Eng. 115 (2017) 1372–1397.
[10] K. Vafai, L. Zhu, Analysis of two-layered micro-channel heat sink concept in electronic cooling, Int. J. Heat Mass Tran. 42 (1999) 2287–2297.
[11] S.H. Chong, K.T. Ooi, T.N. Wong, Optimisation of single and double layer counter flow microchannel heat sinks, Appl. Therm. Eng. 22 (2002) 1569–1585.
[12] Y. Liu, X. Luo, W. Liu, Cooling behavior in a novel heat sink based on muitilayer staggered honeycomb structure, in: International Conference on Micro/Nanoscale Heat Transfer, 2009, pp. 131–135.
[13] P. Dixit, N. Lin, J. Miao, et al., Silicon nanopillars based 3D stacked microchannel heat sinks concept for enhanced heat dissipation applications in MEMS packaging, Sens Actuators A Phys 141 (2008) 685–694.
[14] B. Osanloo, A. Mohammadi-Ahmar, A. Solati, et al., Performance enhancement of the double-layered micro-channel heat sink by use of tapered channels, Appl. Therm. Eng. 102 (2016) 1345–1354.
[15] K.-C. Wong, M.-L. Ang, Thermal hydraulic performance of a double-layer microchannel heat sink with channel contraction, Int. Commun. Heat Mass Tran. 81 (2017) 269–275.
[16] H. Shen, Y. Zhang, C.-C. Wang, et al., Comparative study for convective heat transfer of counter-flow wavy double-layer microchannel heat sinks in staggered arrangement, Appl. Therm. Eng. 137 (2018) 228–237.
[17] E. Khodabandeh, S.A. Rozati, M. Joshaghani, et al., Thermal performance improvement in water nanofluid/GNP–SDBS in novel design of double-layer microchannel heat sink with sinusoidal cavities and rectangular ribs, J. Therm. Anal. Calorim. 136 (2019) 1333–1345.
[18] L. Liu, Z. Cao, C. Xu, et al., Investigation of fluid flow and heat transfer characteristics in a microchannel heat sink with double-layered staggered cavities, Int. J. Heat Mass Tran. 187 (2022) 122535.
[19] S. Sarvar-Ardeh, R. Rafee, S. Rashidi, A comparative study on the effects of channel divergence and convergence on the performance of two-layer microchannels, Exp. Tech. 47 (2023) 109–122.
[20] H. Shen, H. Liu, X. Shao, et al., Thermofluids performances on innovative design with multi-circuit nested loop applicable for double-layer microchannel heat sinks, Appl. Therm. Eng. 219 (2023) 119699.
[21] G. Narendran, B. Mallikarjuna, B.K. Nagesha, et al., Experimental investigation on additive manufactured single and curved double layered microchannel heat sink with nanofluids, Heat Mass Tran. (2023) 1–22.
[22] S. Borah, B. Ranjan Tamuli, D. Bhanja, Thermohydraulic performance intensification of wavy, double-layered microchannel heat sink with height tapering, J Thermophys Heat Trans 37 (2023) 119–132.
[23] A. Goosheneshin, A. Alamdari, P. Setoodeh, Experimental examination of the cooling performance of a cylindrical microchannel heat sink with straight and sinusoidal fins and alumina nanofluid coolant, J. Therm. Anal. Calorim. 147 (2022) 7573–7588.
[24] Y.-T. Yang, H.-W. Tang, W.-P. Ding, Optimization design of micro-channel heat sink using nanofluid by numerical simulation coupled with genetic algorithm, Int. Commun. Heat Mass Tran. 72 (2016) 29–38.
[25] Z.-H. Wang, X.-D. Wang, W.-M. Yan, et al., Multi-parameters optimization for microchannel heat sink using inverse problem method, Int. J. Heat Mass Tran. 54 (2011) 2811–2819.
[26] F. Fakhrabadi, F. Kowsary, Optimal design of a hybrid liquid desiccant-regenerative evaporative air conditioner, Energy Build. 133 (2016) 141–154.
[27] J.-C. Hsieh, D.T.W. Lin, C.-H. Cheng, et al., The optimal design of the thermal spreading on high power LEDs, Microelectronics J 45 (2014) 904–909.
[28] B.S. Kim, B.S. Kwak, S. Shin, et al., Optimization of microscale vortex generators in a microchannel using advanced response surface method, Int. J. Heat Mass Tran. 54 (2011) 118–125.
[29] M. Hatami, D. Song, D. Jing, Optimization of a circular-wavy cavity filled by nanofluid under the natural convection heat transfer condition, Int. J. Heat Mass Tran. 98 (2016) 758–767.
[30] M. Ebrahimi, F. Mahboubi, M.R. Naimi-Jamal, RSM base study of the effect of deposition temperature and hydrogen flow on the wear behavior of DLC films, Tribol. Int. 91 (2015) 23–31.
[31] S. Assarzadeh, M. Ghoreishi, A dual response surface-desirability approach to process modeling and optimization of Al2O3 powder-mixed electrical discharge machining (PMEDM) parameters, Int. J. Adv. Des. Manuf. Technol. 64 (2013) 1459–1477.
[32] I.L. Collins, J.A. Weibel, L. Pan, et al., A permeable-membrane microchannel heat sink made by additive manufacturing, Int. J. Heat Mass Tran. 131 (2019) 1174–1183.
[33] J. Zhang, S. Prakash, Y. Jaluria, et al., An experimental study on the effect of configuration of multiple microchannels on heat removal for electronic cooling, in: International Heat Transfer Conference, 2010, pp. 473–480.
[34] D. Jing, L. He, Thermal characteristics of staggered double-layer microchannel heat sink, Entropy 20 (2018) 537.

[35] J. Zhou, M. Hatami, D. Song, et al., Design of microchannel heat sink with wavy channel and its time-efficient optimization with combined RSM and FVM methods, Int. J. Heat Mass Tran. 103 (2016) 715–724.
[36] J. Zhou, M. Hu, D. Jing, An efficient method for the geometric parameters optimization of double-layer micro-channel heat sink, Numeri Heat Transf A Appl 77 (2020) 966–980.
[37] Y.K. Prajapati, Influence of fin height on heat transfer and fluid flow characteristics of rectangular microchannel heat sink, Int. J. Heat Mass Tran. 137 (2019) 1041–1052.
[38] Wei X, Joshi Y, Patterson MK. Experimental and Numerical Study of a Stacked Microchannel Heat Sink for Liquid Cooling of Microelectronic Devices.
[39] N. Patel, H.B. Mehta, Experimental investigations on a variable channel width double layered minichannel heat sink, Int. J. Heat Mass Tran. 165 (2021) 120633.
[40] P. Bhandari, Y.K. Prajapati, Thermal performance of open microchannel heat sink with variable pin fin height, Int. J. Therm. Sci. 159 (2021) 106609.
[41] G. Xie, Z. Chen, B. Sunden, et al., Numerical predictions of the flow and thermal performance of water-cooled single-layer and double-layer wavy microchannel heat sinks, Numeri Heat Transf A Appl 63 (2013) 201–225.
[42] R.H. Myers, D.C. Montgomery, C.M. Anderson-Cook, Response Surface Methodology: Process and Product Optimization Using Designed Experiments, John Wiley & Sons, 2016.
[43] D.C. Montgomery, Design and Analysis of Experiments, John wiley & sons, 2017.
[44] G. Derringer, R. Suich, Simultaneous optimization of several response variables, J. Qual. Technol. 12 (1980) 214–219.
[45] E. del Castillo, D.C. Montgomery, D.R. McCarville, Modified desirability functions for multiple response optimization, J. Qual. Technol. 28 (1996) 337–345.